Geophysical Research Letters

RESEARCH LETTER
10.1029/2023GL105228

Global Distribution of Climatic Aridity

Jun Yin[1,2] and **Amilcare Porporato**[3,4]

[1]Department of Hydrometeorology, Nanjing University of Information Science and Technology, Nanjing, China, [2]Key Laboratory of Hydrometeorological Disaster Mechanism and Warning of Ministry of Water Resources, Institute of Soil Health and Climate-Smart Agriculture, Nanjing University of Information Science and Technology, Nanjing, China, [3]Department of Civil and Environmental Engineering, Princeton University, Princeton, NJ, USA, [4]High Meadows Environmental Institute, Princeton University, Princeton, NJ, USA

Key Points:

- Exponential variability of precipitation is an essential constraint on the global pattern of climatic aridity as measured by dryness index
- Distribution of dryness index has one parameter quantifying the overall balance between global mean atmospheric water demand and supply
- Dryness index distribution will likely retain its form in future drier climates as projected by Earth System Models

Supporting Information:

Supporting Information may be found in the online version of this article.

Correspondence to:

J. Yin and A. Porporato,
jy12@princeton.edu;
aporpora@princeton.edu

Citation:

Yin, J., & Porporato, A. (2023). Global distribution of climatic aridity. *Geophysical Research Letters*, *50*, e2023GL105228. https://doi.org/10.1029/2023GL105228

Received 4 JUL 2023
Accepted 22 SEP 2023

Author Contributions:

Conceptualization: Jun Yin, Amilcare Porporato
Data curation: Jun Yin
Formal analysis: Jun Yin, Amilcare Porporato
Methodology: Jun Yin, Amilcare Porporato
Writing – original draft: Jun Yin
Writing – review & editing: Jun Yin, Amilcare Porporato

Abstract Aridity exerts fundamental controls on terrestrial hydrology with impacts on ecosystems and society. Here we show that the global distribution of dryness index is dominated by the exponential variability of precipitation. The resulting distribution of the dryness index only has one parameter describing the balance between global mean atmospheric water demand and supply. Its shape, with a minus two power-law tail, is well supported by observations and appears to be robust to future changes in aridity, making it a possible benchmark for Earth System Models.

Plain Language Summary While water availability is of great importance to the ecosystem and society, modeling its distribution at the global scale has large uncertainties. Here we quantify water availability as the dryness index defined as the ratio of long-term averages of atmospheric water demand (potential evapotranspiration) to supply (precipitation). We find the global distribution of the dryness index is essentially controlled by the spatial variations of precipitation. Such distributions did not have significant change in the past century and their shape appears to be robust even for the drier future climates as projected by climate models.

The dryness index, the ratio of long-term averages of atmospheric water demand (potential evapotranspiration, PET) to supply (precipitation, P), provides a fundamental measure of climatic aridity. Based on dimensional analysis (Porporato, 2022), it was originally proposed by Budyko (1974), as a key quantity controlling the long-term hydrological partitioning of precipitation into runoff and evapotranspiration. Since then, it has been widely applied to water resource management (Wisser et al., 2008), crop yield prediction (Bannayan et al., 2010), ecological restoration (Shao et al., 2018), soil microbial activity (Maestre et al., 2015) and disease mapping (Bhatt et al., 2015; Pigott et al., 2014). The global patterns of dryness index in both current and future climates are therefore fundamental for our understanding of the Earth system and are critical for addressing challenges related to food security, ecosystem resilience, and public health.

Space-time patterns of dryness index are complex due to the variability of the hydrometeorological and ecohydrological processes. While these processes have been extensively observed by global networks of ground stations and meteorological satellites, the patterns of the global dryness index have seldom been systematically investigated to provide a theoretical explanation for the global distribution of drylands and wetlands. Future projections of the dryness index are subject to the accuracy of Earth System Models (ESMs), which successively simulate hydrometeorological processes controlled by large-scale circulation but may have large uncertainties in modeling unresolved subgrid processes (Masson-Delmotte et al., 2021). For example, ESMs tend to overestimate precipitation over most regions (Li et al., 2022), underestimate temperatures in the Tibetan Plateau and tropical regions (Fan et al., 2020), and overestimate the decreasing trends of dryness index over central Africa, Sahel region, and the Arabian Peninsula (Chai et al., 2021). As a result, a bottom-up characterization of the global distribution of dryness index starting from detailed spatiotemporal simulations is prone to considerable biases and uncertainties.

A top-down approach, based on capturing the dominant constraints and controls on the global dryness index, is pursued here. Having in mind the definition of the dryness index

$$D_I = \frac{\mathrm{PET}}{P}, \tag{1}$$

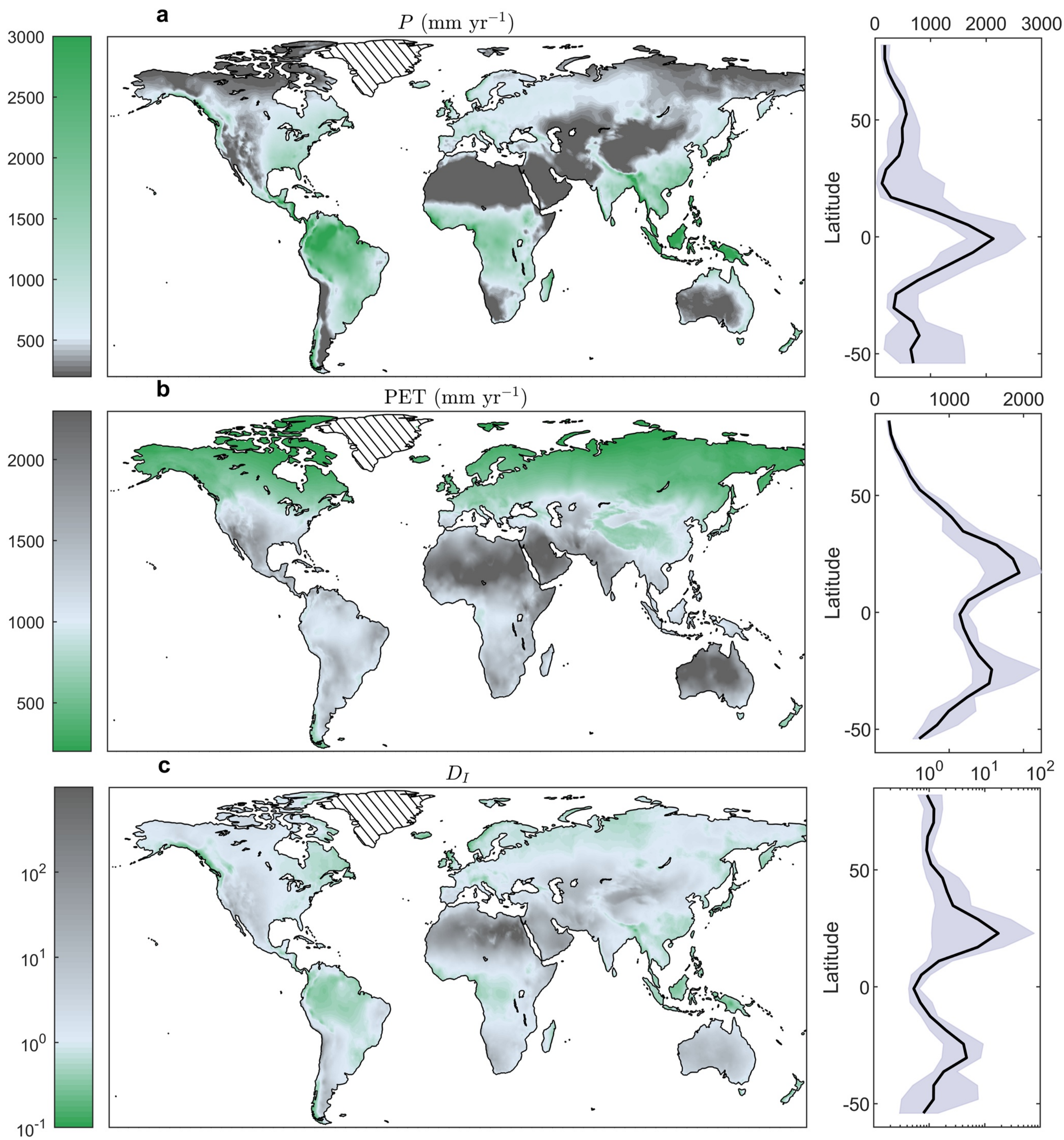

Figure 1. Global precipitation (a, P), potential evapotranspiration (b, PET), and dryness index (c, D_I) over the ice-free lands. Antarctica and Greenland are excluded in this study (hatched areas). The right panels show the interquartile range (shaded areas) and median values (black lines) of the corresponding variables. Global long-term averages of P and PET are obtained from Climatic Research Unit data set.

we first examined the global distributions of long-term averages of P and PET over the ice-free land (see Figure 1). As can be seen, both P and PET are generally smaller at high latitudes, but their maximum values are not in the same locations. The highest P is near the equator, whereas the highest PET is around 25°N and 25°S related to the global desert regions. The resulting D_I has both the largest means and variances near 25°N, where there are both Sahara deserts and humid southeastern China.

10.1029/2023GL105228

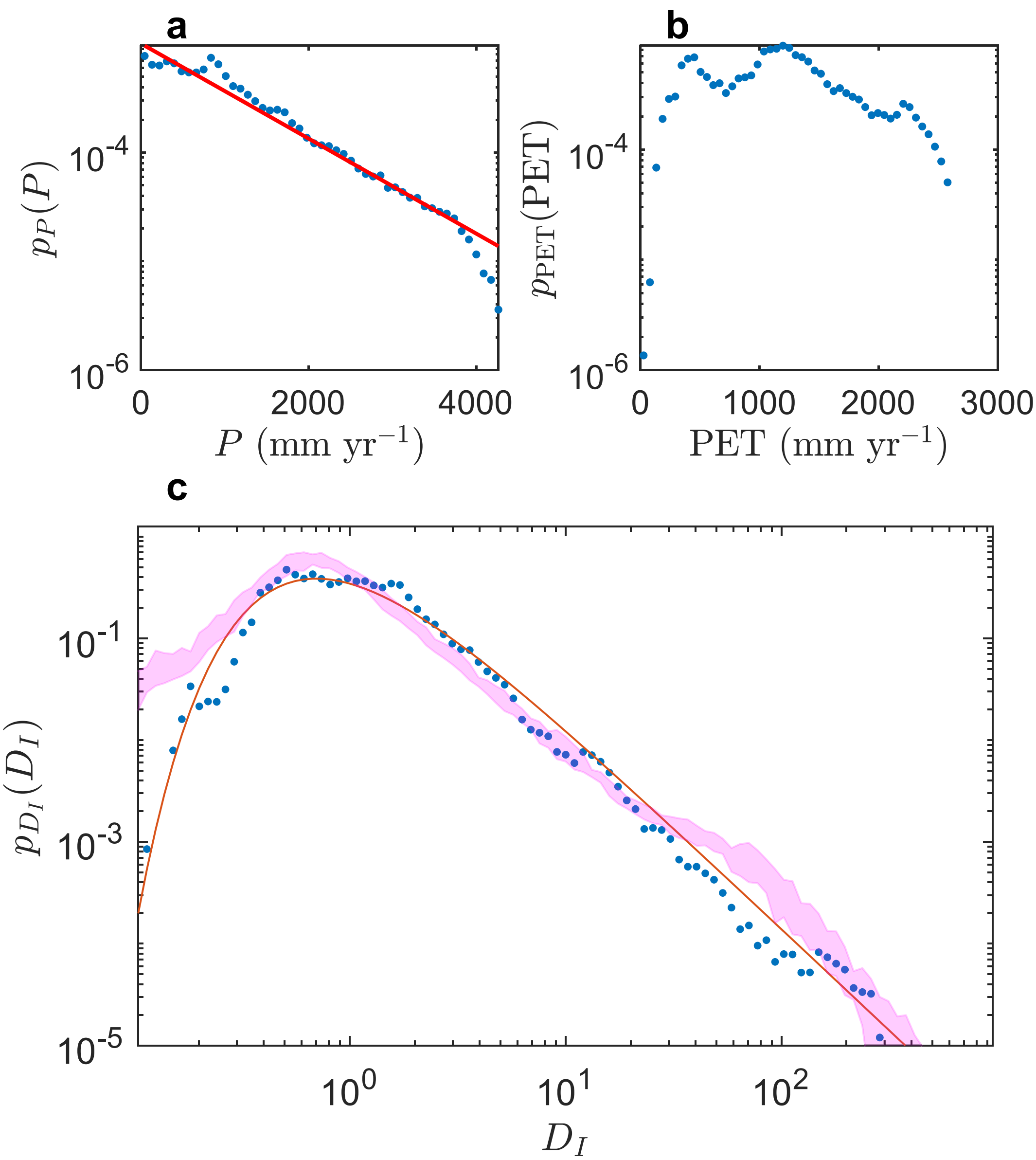

Figure 2. Global distributions of (a) precipitation, (b) potential evapotranspiration, and (c) dryness index over the ice-free lands. Antarctica and Greenland are excluded in this study. The long-term precipitation and potential evapotranspiration over the land were obtained from the Global Precipitation Climatology Project and Climatic Research Unit, respectively. Distributions with other data sources were reported in Figure S2 of Supporting Information S1. The dots and red lines are the empirical distribution from data and the corresponding theoretical distribution. The shading represents the first and third quartiles of the distributions from the Earth System Model outputs (Figures S5 and S6 in Supporting Information S1 present the distributions from each model).

From a statistical point of view (Figures 2a and 2b, and their joint distribution in Figure S1 of Supporting Information S1), annual precipitation appears exponentially distributed over a wide range of values, from almost zero to more than 4,000 mm. Such a distribution suggests that precipitation is a highly stochastic process, consistent with a maximum entropy configuration, giving rise to the largest spatial spread for a given mean (Jaynes, 2003). Conversely, data for PET result in a distribution more concentrated around its global mean value, thus displaying less variability and reduced extremes. Accordingly, with PET dominated by its mean value and P exponentially distributed with mean μ, the theoretical distribution of the global dryness index is obtained (see Text S1 in Supporting Information S1) as a derived distribution (Porporato & Yin, 2022) in the form

$$p_{D_I}(D_I) = \frac{\text{PET}}{\mu D_I^2} e^{-\frac{\text{PET}}{\mu D_I}} = \frac{D_0}{D_I^2} e^{-\frac{D_0}{D_I}}, \tag{2}$$

where the only parameter, $D_0 = \text{PET}/\mu$, is the ratio of the global mean potential evapotranspiration to precipitation, expressing the overall balance between global mean atmospheric water demand and supply. Importantly, as D_I increases, $p_{D_I}(D_I)$ asymptotically approaches $D_0 D_I^{-2}$, displaying a power-law tail with an exponent of −2. The inverse of the dryness index is sometimes referred to as the humidity index, $H_I = P/\text{PET}$ (e.g., Daly et al., 2019; Fu & Feng, 2014; Middleton & Thomas, 1997; Porporato, 2022), and the corresponding distribution can be expressed as

$$p_{H_I} = \frac{1}{H_0} \mathrm{e}^{-\frac{H_I}{H_0}}, \tag{3}$$

where H_0 is the ratio of the global mean precipitation to potential evapotranspiration. Therefore, H_I is theoretically exponentially distributed with mean H_0.

To validate our theory, we used gauge-based and satellite data sets from Climatic Research Unit (CRU) (Harris et al., 2014), Global Aridity Index and Potential Evapotranspiration Database (Version 3, Global AI PET v3) (Zomer et al., 2022), Global Precipitation Climatology Centre (GPCC) (Schneider et al., 2008), and Global Precipitation Climatology Project (GPCP) (Adler et al., 2018). The combinations of the potential evapotranspiration and precipitation data were used to calculate the dryness index over the ice-free lands (see the study domain in Figure 1). We treated these grid data sets as weighted samples with geodetic weights measuring the relative size of each grid and the spatial distribution of global dryness index is evaluated as the weighted histograms (Wei et al., 2022).

All the empirical distributions are well captured by the theoretical distribution in Equation 2 with asymmetric tails and a mode around one (see Figure 2c, Figure S2 in Supporting Information S1, and the distribution of humidity index in Figure S3 of Supporting Information S1). Remarkably, the close match is obtained using only a single physical parameter, the average global dryness index D_0, directly estimated as the ratio of global mean PET to P, following its definition without any calibration. To further test that the variations of PET have limited impacts, we also considered empirical distributions obtained by setting PET as constant and equal to the global mean value. The simplified results still follow the theoretical distributions (see Figure S4 in Supporting Information S1), further highlighting the fact that precipitation acts as an essential constraint on the global patterns of dryness index.

We also analyzed the results from 16 ESMs that participated in Coupled Model Intercomparison Project Phase 6 (CMIP6, see Table S1 in Supporting Information S1). To be consistent with CRU data (Harris et al., 2014), we assumed a reference crop height of 0.12 m and a constant stomatal resistance of 70 s m^{-1}. We used Penman-Monteith equation to calculate PET by using model outputs of surface available energy (sum of "hfls" and "hfss"), relative humidity ("hurs"), near-surface wind speed ("sfcWind"), and near-surface air temperature ("tas"). The 10-m wind speed is converted to the value at 2 m height following the logarithmic wind speed profile assumption (Allen et al., 1998).

We focused on 2005–2014 from "historical" experiments to investigate the long-term average precipitation and PET. The resulting distributions over the ice-free lands also show a power-law tail with an exponent around −2, as predicted by Equation 2. Particularly, most models tend to overestimate the extreme wet regions (i.e., left tails of the distribution). Hence, having a robust distribution supported by data provides a useful benchmark for the global validation of ESMs. It should be noted that various methods have been used for the calculation of PET and thus influence the estimation of D_I. More comprehensive tests from different data sources and methods and detailed explanations of their differences will be the subject of future research.

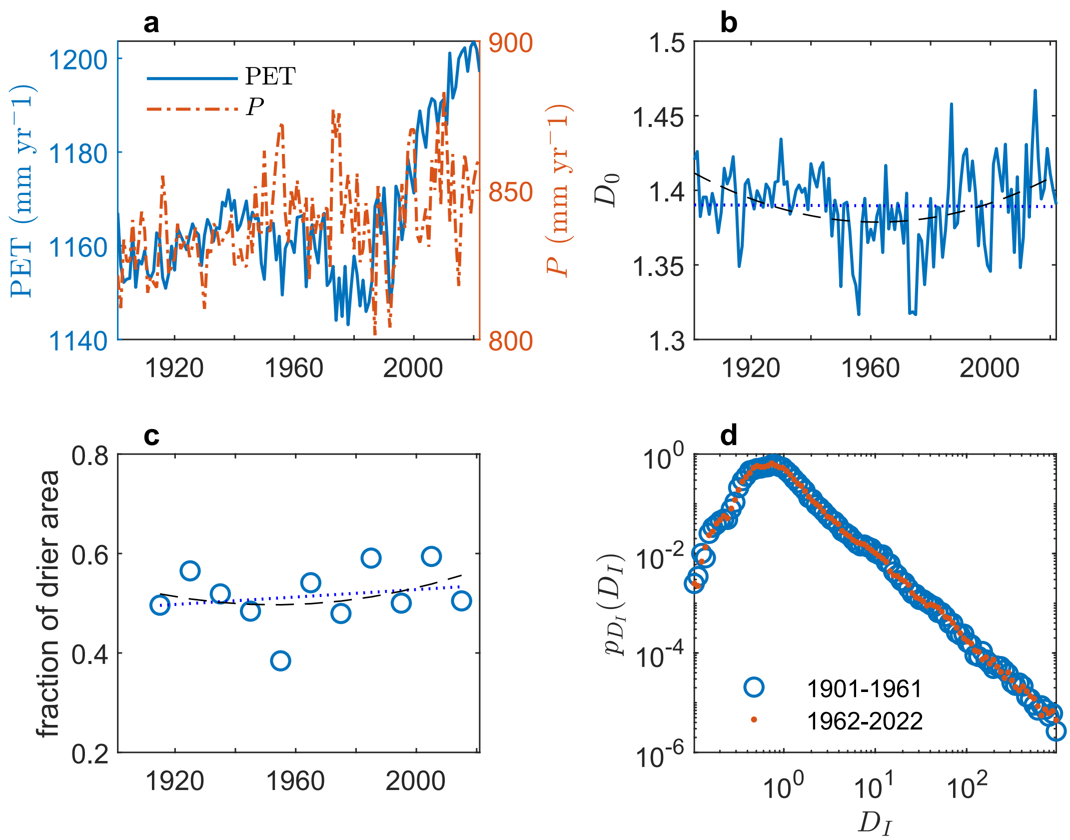

Figure 3. Observed changes in dryness index. (a) Global mean of precipitation and potential evapotranspiration; (b) annual changes in D_0 calculated as the global mean potential evapotranspiration over precipitation; (c) fraction of area with larger dryness in successive decades (e.g., the first circle on the left shows the relative drier area between 1911–1920 and 1901–1910); (d) global distributions of dryness index in two periods of 1901–1961 and 1962–2022 (portions of these distributions for $0 < D_I < 5$ are highlighted in Figure S7 of Supporting Information S1). The dotted line and dash curve in panels b and c refer to the first- and second-order polynomial fits. All results are based on Climatic Research Unit data over the ice-free lands.

The obtained distributions of dryness index may also be of interest for hydroclimatic projections. To address this point, we used both long-term observations from CRU and shared socioeconomic pathway experiments from CMIP6 models. The observations show relatively faster increases in global mean PET than P, particularly after 1970 (Figure 3a). The corresponding D_0, calculated for each year over 1901–2022 and reported in Figure 3b, does not show significant positive or negative trends as assessed by Mann-Kendall statistical tests (p-value = 0.59). The first-order polynomial fit has a very small negative slope, whereas the second-order polynomial fit shows a concave shape. Accordingly, the fractions of areas with larger local dryness index in successive decades also tend to first decrease and then increase (Figure 3c). Due to the very close values of D_0 and very small changes in drier areas between 1901–1961 and 1962–2022, no significant changes in D_I distributions over this 60-year span are visible (Figure 3d), both of which generally follow the theoretical form in Equation 2. These results are consistent with other independent studies (Pan et al., 2021; Ullah et al., 2022), both of which show that global dryland areas

Table 1
Projections of Dryness Index From Earth System Model (ESM) Outputs

Model	(a) $\Delta P/P$	(b) ΔPET/PET	(c) $\Delta D_0/D_0$	(d) Drier area
ACCESS-CM2	0.10	0.21	0.10	0.68
ACCESS-ESM1-5	0.02	0.17	0.14	0.74
CAS-ESM2-0	0.05	0.19	0.13	0.60
CESM2	0.07	0.20	0.13	0.74
CMCC-CM2-SR5	0.11	0.17	0.05	0.64
CanESM5	0.13	0.22	0.08	0.58
CanESM5-1	0.11	0.22	0.10	0.55
FGOALS-f3-L	0.10	0.16	0.06	0.69
FIO-ESM-2-0	0.08	0.18	0.09	0.73
GFDL-ESM4	0.01	0.14	0.13	0.76
INM-CM4-8	0.13	0.10	−0.02	0.50
INM-CM5-0	0.10	0.10	0.00	0.58
IPSL-CM6A-LR	0.08	0.22	0.12	0.74
KACE-1-0-G	0.12	0.18	0.06	0.68
MIROC6	0.07	0.14	0.06	0.76
MRI-ESM2-0	0.07	0.14	0.07	0.63
Mean	0.08	0.17	0.08	0.66

Note. (a–c) The first three columns report the relative changes in global mean P, PET, and D_0 over the ice-free lands between 2000 and 2014 from the "historical" experiment and 2085–2099 from the "ssp585" experiment, whereas the last column shows the fraction of the area in the ice-free lands with a larger dryness index. See Table S1 in Supporting Information S1 for the model names and the corresponding institutes.

and global aridity tend to first decrease and then increase with overall slight decreasing trends over the last century.

For future projections, we also used the Penman-Monteith equation to calculate PET and compared the estimated dryness index from the "historical" experiment during 2000–2014 with those from "ssp585" during 2085–2099. We found that most models project much faster increases of PET than P under warming climates, resulting in approximately 8% higher D_0 over 85 years. Accordingly, nearly 70% of the global land becomes drier with a higher dryness index (see Table 1). These increasing trends of global aridification are consistent with previous studies (e.g., Feng & Fu, 2013; Fu & Feng, 2014; Huang et al., 2016; Scheff & Frierson, 2015; Wang et al., 2021). Even with these marked changes in the hydrometeorological process, the global distributions of D_I however seem to retain similar forms (see Figures S5 and S6 in Supporting Information S1), thus offering a robust perspective on how climatic aridity may change in future climates.

In summary, the theoretical distribution of the dryness index establishes a robust baseline for a wide variety of multidisciplinary studies. Future studies may combine it with the well-known Budyko framework (Budyko, 1974) as the most minimalist model of global hydrology, allowing us to estimate global patterns of surface water and energy partitioning. The long power-law tail, inherited from the dominant role of the exponential rainfall distribution, when combined with local ecohydrological processes, controls the global distributions of drylands. The shorter left tail, which appears to be less accurate in ESMs, is associated with global wetlands. Improving estimates of their distributions in future climates is crucial to model and predict disease spreading, biodiversity threats, and carbon storage in these regions.

Data Availability Statement

Global Aridity Index and Potential Evapotranspiration (ET0) Database can be assessed from Trabucco and Zomer (2019); CRU high-resolution gridded data can be found at Harris (2020); GPCC data can be downloaded from https://psl.noaa.gov/data/gridded/data.gpcc.html (Schneider et al., 2015); GPCP datasets are available at https://psl.noaa.gov/data/gridded/data.gpcp.html (Adler et al., 2003); CMIP6 outputs can be downloaded from https://esgf-node.llnl.gov/search/cmip6/ and CMIP6 models used in this study are listed in Table S1 of Supporting Information S1. Estimated global aridity data were deposited at Yin (2023).

Acknowledgments
J.Y. acknowledges support from the Natural Science Foundation of Jiangsu Province (BK20221343). A.P. acknowledges support from the Carbon Mitigation Initiative at Princeton. The comments and useful criticisms of two anonymous reviewers are gratefully acknowledged.

References

Adler, R. F., Huffman, G. J., Chang, A., Ferraro, R., Xie, P., Janowiak, J., et al. (2003). The version 2 Global Precipitation Climatology Project (GPCP) monthly precipitation analysis (1979–present) [Dataset]. NOAA Physical Sciences Laboratory. Retrieved from https://psl.noaa.gov/data/gridded/data.gpcp.html

Adler, R. F., Sapiano, M. R., Huffman, G. J., Wang, J.-J., Gu, G., Bolvin, D., et al. (2018). The Global Precipitation Climatology Project (GPCP) monthly analysis (new version 2.3) and a review of 2017 global precipitation. *Atmosphere*, *9*(4), 138. https://doi.org/10.3390/atmos9040138

Allen, R. G., Pereira, L. S., Raes, D., & Smith, M. (1998). Crop evapotranspiration-Guidelines for computing crop water requirements-FAO Irrigation and drainage paper 56. *FAO, Rome*, *300*(9).

Bannayan, M., Sanjani, S., Alizadeh, A., Lotfabadi, S. S., & Mohamadian, A. (2010). Association between climate indices, aridity index, and rainfed crop yield in northeast of Iran. *Field Crops Research*, *118*(2), 105–114. https://doi.org/10.1016/j.fcr.2010.04.011

Bhatt, S., Weiss, D. J., Cameron, E., Bisanzio, D., Mappin, B., Dalrymple, U., et al. (2015). The effect of malaria control on *Plasmodium falciparum* in Africa between 2000 and 2015. *Nature*, *526*(7572), 207–211. https://doi.org/10.1038/nature15535

Budyko, M. I. (1974). *Climate and life*. Academic Press.

Chai, R., Mao, J., Chen, H., Wang, Y., Shi, X., Jin, M., et al. (2021). Human-caused long-term changes in global aridity. *Npj Climate and Atmospheric Science*, *4*(1), 1–8. https://doi.org/10.1038/s41612-021-00223-5

Daly, E., Calabrese, S., Yin, J., & Porporato, A. (2019). Hydrological spaces of long-term catchment water balance. *Water Resources Research*, *55*(12), 10747–10764. https://doi.org/10.1029/2019WR025952

Fan, X., Duan, Q., Shen, C., Wu, Y., & Xing, C. (2020). Global surface air temperatures in CMIP6: Historical performance and future changes. *Environmental Research Letters*, *15*(10), 104056. https://doi.org/10.1088/1748-9326/abb051

Feng, S., & Fu, Q. (2013). Expansion of global drylands under a warming climate. *Atmospheric Chemistry and Physics*, *13*(19), 10081–10094. https://doi.org/10.5194/acp-13-10081-2013

Fu, Q., & Feng, S. (2014). Responses of terrestrial aridity to global warming. *Journal of Geophysical Research: Atmospheres*, *119*(13), 7863–7875. https://doi.org/10.1002/2014JD021608

Harris, I. (2020). Climatic Research Unit (CRU) Time-Series (TS) version 4.03 of high-resolution gridded data. [Dataset]. Climatic Research Unit: Data. https://crudata.uea.ac.uk/cru/data/hrg/

Harris, I., Jones, P. D., Osborn, T. J., & Lister, D. H. (2014). Updated high-resolution grids of monthly climatic observations - The CRU TS3.10 dataset: Updated high-resolution grids of monthly climatic observations. *International Journal of Climatology*, *34*(3), 623–642. https://doi.org/10.1002/joc.3711

Huang, J., Yu, H., Guan, X., Wang, G., & Guo, R. (2016). Accelerated dryland expansion under climate change. *Nature Climate Change*, *6*(2), 166–171. https://doi.org/10.1038/nclimate2837

Jaynes, E. T. (2003). *Probability theory: The logic of science*. Cambridge University Press.

Li, Z., Liu, T., Huang, Y., Peng, J., & Ling, Y. (2022). Evaluation of the CMIP6 precipitation simulations over global land. *Earth's Future*, *10*(8), e2021EF002500. https://doi.org/10.1029/2021EF002500

Maestre, F. T., Delgado-Baquerizo, M., Jeffries, T. C., Eldridge, D. J., Ochoa, V., Gozalo, B., et al. (2015). Increasing aridity reduces soil microbial diversity and abundance in global drylands. *Proceedings of the National Academy of Sciences*, *112*(51), 15684–15689. https://doi.org/10.1073/pnas.1516684112

Masson-Delmotte, V., Zhai, P., Pirani, A., Connors, S. L., Péan, C., Berger, S., et al. (2021). Climate change 2021: The physical science basis. Contribution of Working Group I to the Sixth Assessment Report of the Intergovernmental Panel on Climate Change (Vol. *2*).

Middleton, N., & Thomas, D. S. (1997). *World atlas of desertification* (Vol. 182). Arnold London.

Pan, N., Wang, S., Liu, Y., Li, Y., Xue, F., Wei, F., et al. (2021). Rapid increase of potential evapotranspiration weakens the effect of precipitation on aridity in global drylands. *Journal of Arid Environments*, *186*, 104414. https://doi.org/10.1016/j.jaridenv.2020.104414

Pigott, D. M., Golding, N., Mylne, A., Huang, Z., Henry, A. J., Weiss, D. J., et al. (2014). Mapping the zoonotic niche of Ebola virus disease in Africa. *Elife*, *3*, e04395. https://doi.org/10.7554/eLife.04395

Porporato, A. (2022). Hydrology without dimensions. *Hydrology and Earth System Sciences*. https://doi.org/10.5194/hess-2021-442

Porporato, A., & Yin, J. (2022). *Ecohydrology: Dynamics of life and water in the critical zone*. Cambridge University Press. Retrieved from www.cambridge.org/ecohydrology

Scheff, J., & Frierson, D. M. W. (2015). Terrestrial aridity and its response to greenhouse warming across CMIP5 climate models. *Journal of Climate*, *28*(14), 5583–5600. https://doi.org/10.1175/JCLI-D-14-00480.1

Schneider, U., Becker, A., Finger, P., Meyer-Christoffer, A., Rudolf, B., & Ziese, M. (2015). GPCC full data monthly product version 7.0 at 0.5 degree: Monthly land-surface precipitation from rain-gauges built on GTS-based and historic data [Dataset]. Global Precipitation Climatology Centre (GPCC). https://doi.org/10.5676/DWD_GPCC/FD_M_V7_050

Schneider, U., Fuchs, T., Meyer-Christoffer, A., & Rudolf, B. (2008). *Global precipitation analysis products of the GPCC* (p. 112). Global Precipitation Climatology Centre (GPCC), DWD, Internet Publikation.

Shao, Y., Zhang, Y., Wu, X., Bourque, C. P.-A., Zhang, J., Qin, S., & Wu, B. (2018). Relating historical vegetation cover to aridity patterns in the greater desert region of northern China: Implications to planned and existing restoration projects. *Ecological Indicators*, *89*, 528–537. https://doi.org/10.1016/j.ecolind.2018.02.035

Trabucco, A., & Zomer, R. (2019). Global aridity index and potential evapotranspiration (ET0) database: Version 3 [Dataset]. Figshare. https://doi.org/10.6084/m9.figshare.7504448.v5

Ullah, S., You, Q., Sachindra, D. A., Nowosad, M., Ullah, W., Bhatti, A. S., et al. (2022). Spatiotemporal changes in global aridity in terms of multiple aridity indices: An assessment based on the CRU data. *Atmospheric Research*, *268*, 105998. https://doi.org/10.1016/j.atmosres.2021.105998

Wang, X., Jiang, D., & Lang, X. (2021). Future changes in Aridity Index at two and four degrees of global warming above preindustrial levels. *International Journal of Climatology*, *41*(1), 278–294. https://doi.org/10.1002/joc.6620

Wei, R., Li, Y., Yin, J., & Ma, X. (2022). Comparison of weighted/unweighted and interpolated grid data at regional and global scales. *Atmosphere*, *13*(12), 2071. https://doi.org/10.3390/atmos13122071

Wisser, D., Frolking, S., Douglas, E. M., Fekete, B. M., Vörösmarty, C. J., & Schumann, A. H. (2008). Global irrigation water demand: Variability and uncertainties arising from agricultural and climate data sets. *Geophysical Research Letters*, *35*(24), L24408. https://doi.org/10.1029/2008GL035296

Yin, J. (2023). Global aridity data [Dataset]. Zenodo. https://doi.org/10.5281/zenodo.7831607

Zomer, R. J., Xu, J., & Trabucco, A. (2022). Version 3 of the global aridity index and potential evapotranspiration database. *Scientific Data*, *9*(1), 409. https://doi.org/10.1038/s41597-022-01493-1